Journal of Thermal Science

https://doi.org/10.1007/s11630-021-1440-5

Experimental and Numerical Analysis of Cavity/Mean-Flow Interaction in Low Pressure Axial Flow Turbines

BARSI Dario*, COSTA Carlo, LENGANI Davide, SIMONI Daniele, VENTURINO Giulio, ZUNINO Pietro

DIME - Università di Genova, Via Montallegro 1, I-16145 Genova

Abstract: The increasing performance of modern aeroengines led the research towards the optimization of machine components not deeply analyzed in the past. In this context, the mechanisms driving the interaction process between the secondary flows evolving at the hub of low-pressure turbines with the rotor-stator cavity systems have been poorly investigated in the literature. In this work, an experimental and numerical analysis of the interaction between the endwall near wall flow and the leakage flow of a real cavity system is presented. The experimental results were carried out in the annular low-pressure axial flow turbine of the University of Genova. Experimental blade loading and pressure distributions into the cavity, as well as the measured total pressure loss coefficient, have been used for a proper validation of CFD results. Both steady and unsteady calculations were carried out through the commercial solver Numeca. Particularly, several numerical approaches have been tested into this work: RANS, Non Linear Harmonic (NLH), and URANS. The most promising CFD techniques have been firstly identified by comparison with experimental results and then systematically employed to extend the analysis of secondary flow-cavity flow interaction to positions and quantities not available from the experiments. Losses characterizing the mean flow-cavity flow interaction process will be shown to cover a great amount of the overall stage losses and should be properly accounted for the design of future optimized cavity configurations.

Keywords: axial flow turbine, cavity mean-flow interaction, experimental analysis, CFD

1. Introduction

The main goals of a cavity system concern with the optimization of the thermal stratification of the hot gases ingested from the flow path, minimization of the by-pass flow rate and on the research of the optimal interaction process between the mean flow evolving at the hub of the passage and the flow entering/leaving the cavity system. A simple scheme describing the flow developing into the cavity is given in Coren et al. [1], while in Fig. 1 the meridional section of the cavity system tested in the present work is reported.

Daily and Nece [2] have analyzed the flow behavior generated by the rotation of a disk within a simplified cavity geometry, observing that when the cavity passage height is large compared to the outer radius of the rotating disk, an inviscid core flow region generates within the cavity. The flow behavior within the cavity is dominated by the leakage flow and by the rate of flow that is entrained into the rotor disk boundary layer and pumped radially by centrifugal forces. Typically, the coolant flow is supplied into the cavity space to prevent

Received: Nov 15, 2019
AE: BRANDSTETTER Christoph
Corresponding author: BARSI Dario
E-mail: dario.barsi@unige.it

Nomenclature

C_p	pressure coefficient	y	tangential coordinate/m
$C_{p,t}$	total pressure coefficient	y^+	non-dimensional wall coordinate
CFD	Computational Fluid Dynamics	**Greek symbols**	
g	pitch/m	ω	loss coefficient
k	turbulent kinetic energy/$m^2 \cdot s^{-2}$	**Subscripts**	
NHL	Non Linear Harmonic	0	reference value
p	pressure/Pa	HUB	at hub section
R	radial coordinate/m	IN	inlet section
RANS	Reynolds Average Navier Stokes	max	maximum
SST	Shear Stress Transport	OUT	outlet section
T	period/s	s	static
t	time/s	TIP	at tip section
URANS	Unsteady Reynolds Average Navier Stokes	t	total

the thermomechanical failure of the disk and to reduce ingestion of hot gas from the main annulus, thus making the flow field into the cavity even more complex. As the coolant flow rate is increased, the core flow diminishes and then it is definitely suppressed (see Refs. [3] and [4]). The effects of the Reynolds number on the flow behavior within the cavity is analyzed in Zimmermann and Wolff [5], showing that the Reynolds number influence is limited to the case characterized by laminar flows into the cavity, i.e., for low Reynolds numbers.

The effect of different cooling entrance geometries on the flow vortices within the cavity has been analyzed through computational methods by Da Soghe et al. [6], giving evidence of the importance of the effect of disk pumped flow. Coren et al. [7] carried out an extensive experimental investigation to evaluate the influence of several cooling flow parameters such as flow trajectory, jet momentum and flow rate on cooling effectiveness. Guida et al. [8] investigated the cavity flow developing in the new designed test facility of the University of Genova in order to study the influence of Reynolds and Rossby numbers and cooling mass flow rate on the overall performance parameters of the cavity system, like the discharge coefficient and the overall stage efficiency. The evaluation of the discharge coefficient of a seal geometry similar to a real engine one, reproducing the stator-rotor inlet and outlet disk cavities, was also reported in Kong et al. [9]. Willemborg et al. [10] have also studied the influence of different cavity geometries on the discharge coefficient. In order to extent the data fields, several computational works have been carried out in the past. Some of them were validated by experimental data obtained in facilities such as the one in the University of Sussex (MAGPI project) or the one in the University of Genova (E-Break project). Several articles [11, 12] presented works with the aim of comparing different unsteady solutions methods. The validation studies include both single stage and rotor-stator interaction domains. Green et al. [11] compared the results provided by phase-lag method and NLH method on a single stage high pressure turbine geometry. The two models produce similar results, but the phase-lag solution requires ten times of the NLH calculation time, while the NLH requires five times of the phase-lag computational resources. Hembera et al. [12] proves that the NLH method seems to be very promising for fast quasi-unsteady CFD simulation in multi stage turbomachinery. They established the limit of this method in the inability of shock-wave evaluation.

Instead, the effects of different seal geometries on hot-gas ingestion and total pressure loss in a low-pressure turbine were investigated in Schuler et al. [13]. Andreini et al. [14] have studied the interaction effects between main annulus and disk cavities flows, while Coren et al. [15] studied the influence of turbine stator well coolant flow rate and passage configuration on cooling effectiveness. Those calculations prove that the rim seal interaction is dominated by the unsteady Kelvin-Helmoltz type interaction and the potential field of the rotor, as such the exact sealing boundary is not expected to be predicted (the cause of the RANS approach is not well suited). Unsteady calculations by Andreini et al. [14] show also that the main annulus unsteadiness (linked to the wake ingestion) affects only the upper zone of the cavity. Barakos et al. [16] have performed a high speed turbulent cavity flows analysis in order to evaluate the shear layer effect on noise generation. Alexiou et al. [17] have proposed a thermal modelling of an experimental multiple cavity rig aimed to obtain the transient temperature distribution within the cavity. Buron et al.

[18] conducted a study of the rotor-stator interaction by a CFD calculation with the NLH method. The results show that an NLH calculation with two harmonic requires quite the same amount of time of a steady calculation. A four harmonic calculation requires 35% more than two harmonic calculation. Moreover, Gao et al. [19] found that increasing the CFD sector size has little influence on the prediction accuracy of the mean flow distribution.

In the present work, an engine-like cavity system has been studied extensively both experimentally and numerically. The aims of this paper are to provide the most efficient computational technique to analyze the main thermodynamic and kinematic properties of the flow into the cavity and evaluate the effects of the interaction between the main flow and the flows entering/leaving the cavity. CFD results are compared with experimental data to identify the best strategy to model the cavity system. Then the numerical analysis is extended to positions and quantities not available from the experiments. This also allows the computation of the overall loss due to mixing and shear strain interaction between the main flow and the cavity flow for the whole extension of the turbine stage, up to the entrance section of the downstream rotor blade.

2. Experimental Test Rig

The experimental results have been obtained in the annular low-pressure axial flow turbine of the University of Genova. It is a cold flow rig that uses atmospheric air as working fluid. The test section is equipped with a cavity geometry reproducing an engine-like configuration with a scale ratio of 1.5:1. The rotor blades are simulated through bars. Upstream bars have a smaller diameter since they have to simulate the effects due to the turbulence level into the upstream rotor wake, while bars of a significantly larger diameter have been used for the second rotor in order to properly reproduce potential effects coming from downstream. The rotor/stator blade count ratio is 4:3 in order to allow a reduced domain representation in numerical calculations by employing periodic conditions. In Fig. 1, a meridional view of the test section is presented. The leakage flow, coming from the main channel, enters into the cavity from the left and, after evolving into the cavity volume, it interacts with the main flow at the exit section of the cavity. In order to survey the flow evolution into the cavity, the static surfaces of the “T-bar” have been instrumented by means of pressure probes and thermocouples.

Moreover, the locations of the upstream and downstream traverses for the insertion of the Kiel probe (blue lines marked as short domain) are also displayed in Fig. 1. Available experimental data concern pressure distributions into the cavity, total pressure distributions upstream and downstream of the vane and estimation of the discharge coefficient of the cavity for different operating conditions. These data have been used for a proper validation of CFD results. A complete description of the experimental test rig, and the response of the overall efficiency as a function of the parameters variation could be found in the work of Guida et al. [8] and Guida et al. [20].

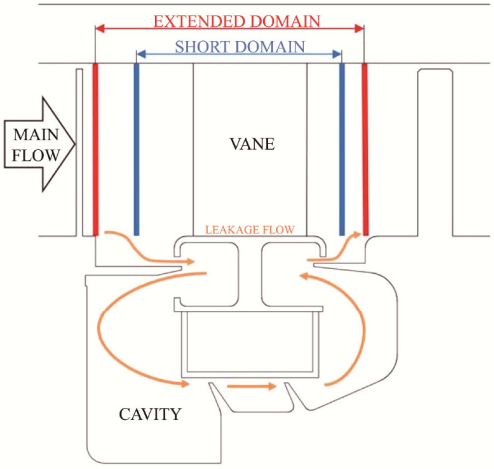

Fig. 1 Meridional view of the test section

3. Numerical Model

The experimental cavity test rig has been modeled in order to carry out numerical simulations. For the mesh generation, Autogrid5 is used in order to realize a structured multi-block mesh for the main channel and for the cavity flow regions. The four blade rows constituting the experimental rig, i.e., the upstream inlet guide vane, the upstream bars, the stator row and the downstream bars, have been discretized with O-4-H type grids. The O-4-H type grids consist of an O-shaped block around the blade surrounded by four H-shaped blocks. The height of the first cell near the solid walls was chosen, for each row, so that the value of the non-dimensional wall coordinate y^+ was around one. The cavity geometry is meshed through the “Meridional effect” feature of Autogrid, which allows generating good quality mesh for axisymmetric complex geometries by filling the domain with several structured 2D blocks. Also for this case, the first cell height is properly chosen in order to correctly evaluate the behavior of the flow field through the teeth present inside the cavity, where the characteristic dimensions of the crossing section are considerably reduced. In Fig. 2, a meridional sketch of the axisymmetric mesh generated for the cavity is presented, where the grid refinement within the narrow teeth passages is clearly visible.

The interfaces between the main channel and the

cavity grids are set as full matching conditions, while the mixing plane approach has been adopted to manage the passage of information from the stator frame to the rotor frame for the steady computations. Both steady and unsteady calculations are carried out by employing the commercial solver Numeca. The discretization in space is based on a cell centered control volume approach, while a Multi stage Runge-Kutta scheme with local time stepping is adopted for time discretization, associated with multigrid technique [21]. For the steady calculation, a RANS approach was used. NLH and URANS calculations were also carried out. The RANS and NLH calculations need a single passage mesh. This is due to the mixing plane approach for RANS and because of the transposition to the frequency domain for the NLH. Instead, URANS calculation needs the representation of four stator blades and three rotor bars (in order to preserve periodicity), given the 4:3 rotor/stator ratio of the present geometry. NLH method decomposes the unsteady flow variables into time-averaged quantities and periodic unsteady perturbations. The unsteady flow field is computed by means of the Fourier decomposition of the periodic fluctuations based on a pre-selected number of harmonics, typically associated with the blade passing frequencies of the turbomachinery configuration and their higher order harmonics. The boundary conditions set for the calculations are the same for all the cases. At the inlet, total quantities are imposed, while at the outlet section a mass flow rate, corresponding to the nominal condition, is set. For turbulence modeling, a SST model has been employed [22]. For the shroud and for the stator surfaces, a static wall boundary condition is imposed. For the rotating parts, as the hub and the bar surfaces, rotating boundary conditions are imposed. The numerical values of boundary condition settings are reported in Table 1.

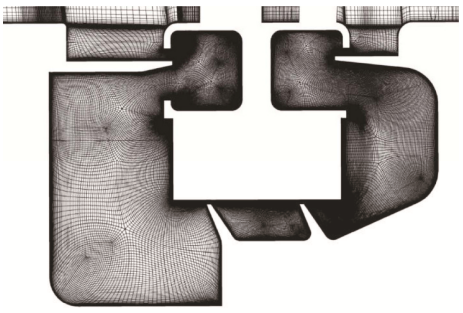

Fig. 2 Meridional representation of the mesh into the cavity

For the grid dependency evaluation, three grids with increasing number of elements have been generated and tested. The parameter used as test variable for the grid dependency is the leakage mass flow rate passing through the cavity. The values found for three different grid refinements are reported in Table 2.

Table 1 Boundary conditions

	Quantity	Value
Inlet	Total pressure/Pa	101 325
	Total temperature/K	297
	Pitch angle/deg	0
	Yaw angle/deg	0
	$k/m^2 \cdot s^{-2}$	13
	$\varepsilon/m^2 \cdot s^{-3}$	2000
Outlet	Mass flow rate/kg·s^{-1}	3.02
	First guess static pressure/Pa	75 000

Table 2 Grid dependency results

	Grid 1	Grid 2	Grid 3
Cell number	7.8 millions	10.3 millions	13.0 millions
Leakage mass flow rate/kg·s^{-1}	3.267×10^{-3}	3.288×10^{-3}	3.290×10^{-3}

Since the values calculated for Case 2 and Case 3 are very similar to each other, the grid 2 was chosen as reference mesh for the successive calculations. For the NLH method, 3 harmonics were solved. For the URANS method, 60 angular positions were simulated. The numerical settings for the calculation are described in Table 3.

Table 3 Numerical settings

	Steady iteration	Sub iteration	Coarse grid iteration	Harmonic number
RANS	3000	–	1000	–
NLH	1500	30	1000	3
URANS	1500	60	1000	–

For the unsteady calculations, ten periods have been computed before start collecting data for further post processing and analysis. This condition allows reaching convergence both for NLH and URANS calculations. In Table 4 the simulation time for the three different numerical approaches is presented.

Table 4 Convergence times

	Convergence time/h
RANS	4
NLH	25
URANS	480

4. Results and Discussion

In order to provide evidence of the capability of the different numerical schemes in reproducing correctly the flow, the pressure distributions into the cavity have been plotted in Fig. 3.

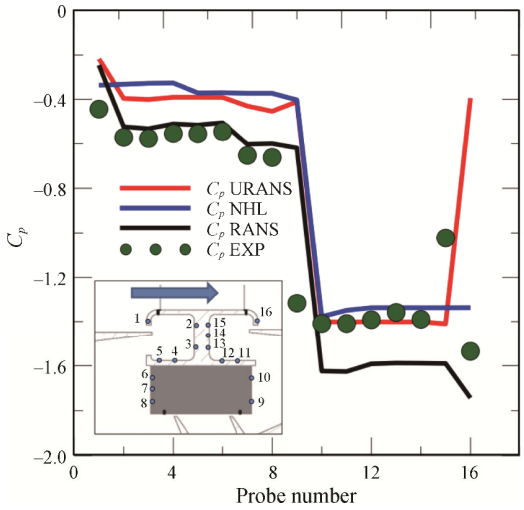

Fig. 3 Cavity pressure coefficient distributions

The cavity pressure coefficient, indicated with C_p, is displayed in the ordinate, while in the abscissa the probe number is presented. This pressure coefficient is made dimensionless with the pressure drop at the vane tip. The experimental curve (green dots) basically makes evident that the pressure level is fairly constant in the first portion of the cavity, prior to that the flow enters into the teeth (located in correspondence of the probe number 8). Across the teeth, the flow experiments all the pressure drop, and keeps again constant the pressure level up to the outlet section of the cavity (probe number 16). As can be noted, the implemented numerical methods gave similar trends for the pressure distribution into the cavity, with some local differences. In particular, it can be observed that:

(1) the RANS approach correctly estimates the first and the second pressure drops experimented by the fluid passing through the first horizontal tooth (from probe 1 to probe 2) and from the first to the second chamber (from probe 5 to probe 6) respectively, while overestimates the second pressure drop through the teeth (from probe 8 to probe 9).

(2) the NLH and URANS approaches underestimate the pressure level in the fore part of the cavity, prior than the teeth. Conversely, these methods correctly estimate the pressure level behind the teeth.

(3) all the numerical approaches overestimate the overall pressure drop with respect to the experimental value.

The third phenomena could be caused by the ingestion of the wake into the cavity, an unsteady phenomenon difficult to be modelled. However, the pressure distribution after the lamination is correctly represented by the two unsteady methods. In order to provide the overall effects due to the cavity flow/main flow interaction in term of stage efficiency, the total pressure loss coefficient radial distribution, computed as:

$$C_{p,\mathrm{t}} = \frac{p_{\mathrm{t,IN}}(y,R) - p_{\mathrm{t,OUT}}(y,R)}{p_{\mathrm{t},0} - p_{\mathrm{s,OUT}}} \tag{1}$$

with values measured/calculated on the blue lines reported in Fig. 1, are reported in Fig. 4.

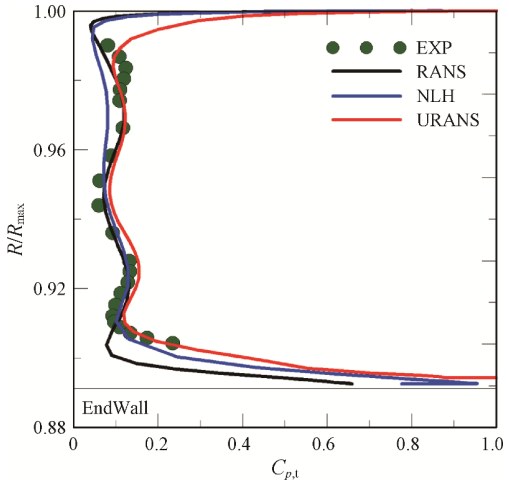

Fig. 4 Vane downstream total pressure loss coefficient

Experimental data (green dots) highlight that the interaction between the secondary flows downstream of the vane and the fluid structures that come from the cavity causes an high loss generation. Indeed, the loss level in the proximity of the hub (R/R_{max}=0.91) becomes significantly higher than the midspan losses. The high values of $C_{p,t}$ observed near to the outlet radius of the cavity are linked to a low momentum flow generated as a consequence of the interaction between the secondary flow structures of the vane developing in the main flow at the hub and the flow leaving the cavity. From a computational point of view, the RANS results have a good matching with the experimental data in the core part of the passage, but they show quite different results in the hub zone. The NLH method provides a good comparison with experimental data also in the shroud region, even though it seems to underrate the low momentum close to the hub. The URANS approach gives the best fit, as provided by the excellent agreement near the hub zone and the reasonable representation close to endwall losses, where secondary flows and the cavity flows are interacting with the endwall boundary layer. However, the NLH method provides appreciable results and allows saving time (there is a factor 20:1 between URANS and NLH computational time), so it could be also considered a reasonable tool for analysis in which the main goal is the computation of global parameters. Then, once verified the computational accuracy through the experimental validation, CFD results have been used to evaluate the dynamic interaction between the main flow and the flow leaving the cavity downstream the vane, thus providing further insight into

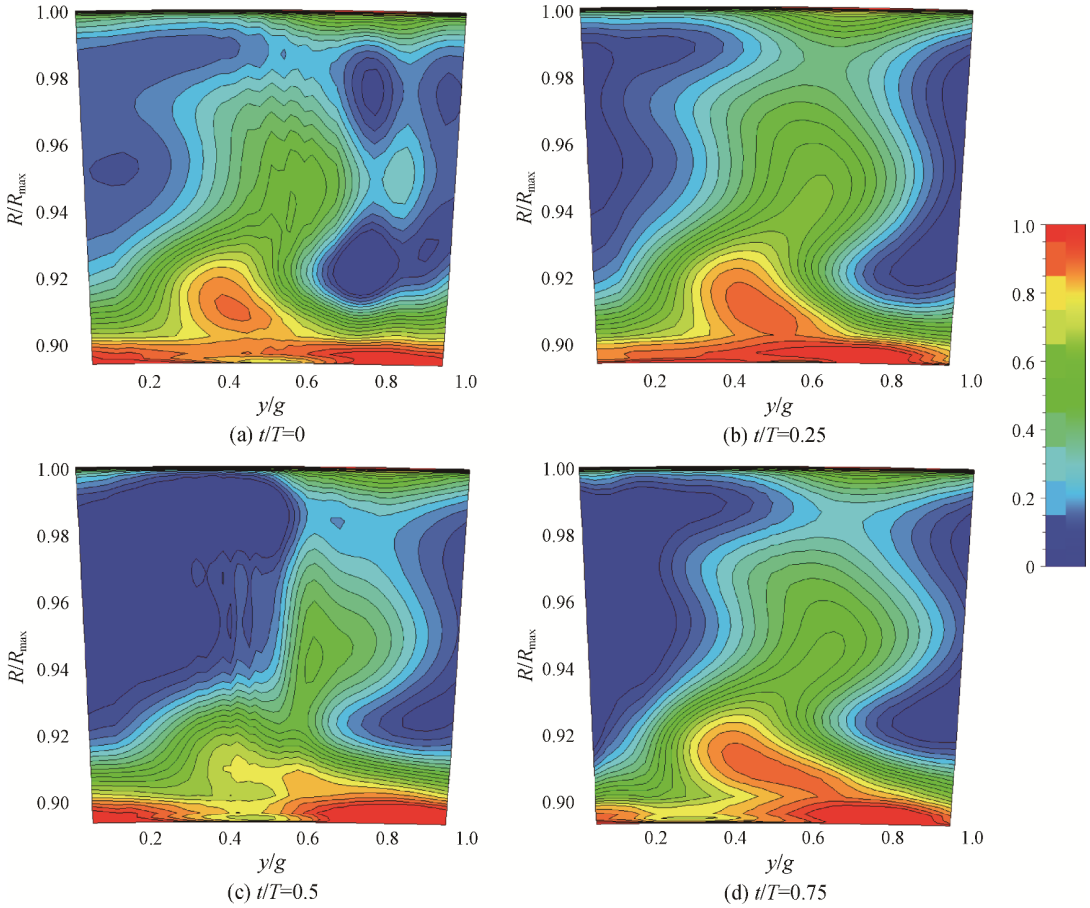

Fig. 5 Time depending total pressure loss coefficient at vane outlet

the process responsible for loss generation. Fig. 5 shows the total pressure loss coefficient obtained by URANS calculation at vane outlet for four different times in the same period.

From these figures it is possible to observe the regions characterized by high losses (and therefore high total pressure coefficient values) near the hub and shroud surfaces. At t/T=0.5, the loss core due to the secondary flows of the vane can be clearly recognized at y/g=0.4, R/R_{max}=0.91. Moreover, the total pressure loss induced by the stator blade wake is clearly visible in the center of the figure. The shape of these high loss regions is altered in time by the action of several effects:

(1) the unsteady wakes effect induced by the upstream rotor bars, that is well known from literature to alter the blade boundary layer transition process.

(2) the potential effect induced by the downstream rotor bars, that induces a time-dependent interaction of the main flow with the one leaving/entering the cavity outlet.

As can be seen, the flow associated to the cavity, characterized by a high value of the total pressure coefficient (red colored zones) due to the losses experienced by the fluid passing through the cavity, massively interacts with main flow, modifying the secondary flow structures. The worst interaction phase occurs at t/T=0.25, with the low momentum fluid exiting from the cavity that produces enlarged loss region close to the hub (from y/g=0.4 to y/g=0.8). In addition, also the loss core due to the secondary flow appears enlarged.

At t/T=0.5, the profile wake appears very thin, as it occurs during the interaction with the upstream rotor wake (see Infantino et al. [23] for instance). At the same time, also the high loss core at the hub appears evidently reduced and the secondary loss core disappeared. At t/T=0.75, the secondary loss core stats growing again, even though the loss region close to the hub is partially suppressed ($0.2<y/g<0.4$) due to a local sucking of flow re-ingested into the cavity. In order to better quantify the effects of this interaction, CFD data obtained by the URANS method have been also used to compute the overall losses generated by the interaction itself, extending the control volume for the computation of the loss level up to the leading edge of the downstream rotor. The red lines in Fig. 1 clearly highlight the further extension of the control volume to the leading edge of the following rotor blade. This allows quantifying the overall losses generated by the leakage flow interacting with the main flow in the whole stage. Fig. 6 shows the pitchwise averaged total pressure loss coefficient computed by the URANS approach for the two axial positions

corresponding to the short and the extended domain indicated in Fig. 1.

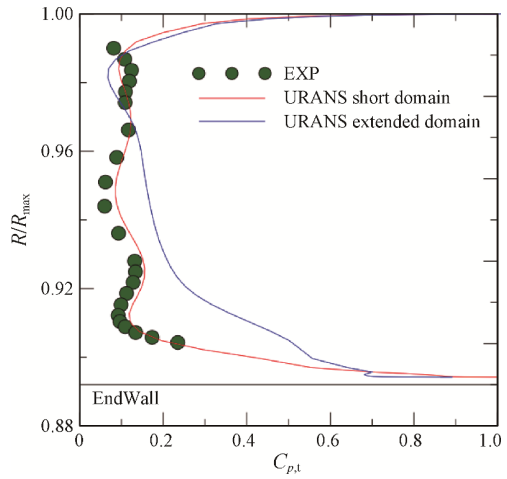

Fig. 6 Pitchwise averaged total pressure loss coefficients for short and extended domains

This figure shows the modification of the total pressure loss coefficient in the axial direction. The interactions and mixing between the cavity flow and the main flow (downstream section) and the effect of hub boundary layer (upstream section) lead to an increase of the $C_{p,t}$, as made evident by the significant enlargement of the loss region characterizing the blue curve in the near-to-the-endwall region.

Data shown in Table 5 present the overall loss level in the two axial positions previously described, calculated as:

$$\omega = \int_{R_{HUB}}^{R_{TIP}} \int_{0}^{g} C_{p,t}(y,R)\, R\,dy\,dR \qquad (2)$$

Table 5 Loss level for short and extended domain

	Short domain	Extended domain
ω	6.74	10.02

Data in Table 5 makes evident that the losses measured in the short domain increases significantly prior to enter the downstream row. The unsteady interaction observed in Fig. 6 is responsible for high deformation work in the hub region. The present results clearly exhibit the possible advantage in optimizing such an unsteady interaction process by means of advanced geometrical configurations.

5. Conclusions

An extensive numerical analysis was conducted in order to study the efficiency of a real stage including the cavity system, as well as to identify the proper numerical scheme able to accurately describe the overall stage efficiency parameters. To this end, three different methods were implemented and tested based on comparison with available experimental results.

Considering the representation of the pressure distribution within the cavity and the total pressure coefficient distribution measured downstream the vane, the URANS method, as expected, has been proved to be the most accurate. However, the NLH method, despite a lack in accuracy, is able to reproduce the general data trend and the overall performance value with an acceptable approximation, and its convergence time is about a twentieth of the URANS one. The time-mean pitchwise averaged total pressure loss coefficient predicted by the URANS method practically coincides, also in the close-to-the-hub region, with the experimental data. This strengthenes the ability of this CFD method to well reproduce the main flow/cavity flow interaction process, which is responsible for the generation of a large amount of losses. CFD results have been also used to compute the overall loss level characterizing the whole stage, up to the leading edge of the downstream rotor. Particularly, the loss level increases significantly passing form a short domain (corresponding to the measurement setup) to the extended one, that cover the whole stage. Those results could lead the future works on the research of methods able to reduce those losses optimizing the cavity flow interaction process.

Acknowledgements

The research leading to these results has received funding from the European Union Seventh Framework Program FP7/2007-2013 under grant agreement No. ACP2-GA-2012-314366-E-BREAK. The authors also wish to acknowledge the MIUR for founding the rig realization and the industrial partners that collaborated through the entire activity, Blue Engineering s.r.l. for the rig design, Progesa s.r.l. for the manufacturing and GE AvioAero for supporting the test program.

References

[1] Coren D., Atkins N., Turner J., Eastwood D., Davies S., Childs P., Dixon J., Scanlon T., An advanced multi-configuration stator well cooling test facility. ASME Turbo Expo 2010: Power for Land, Sea, and Air, Volume 4: Heat Transfer, Parts A and B, Paper No. GT2010-23450, pp. 1259–1270.

[2] Daily J.W., Nece R.E., Chamber dimension effects on induced flow and frictional resistance of enclosed rotating disks. Journal of Basic Engineering, 1960, 82(1): 217–230.

[3] Gartner W., A prediction method for the frictional torque of a rotating disc in a stationary housing with

superimposed radial outflow. ASME 1997 International Gas Turbine and Aeroengine Congress and Exhibition, Volume 3: Heat Transfer; Electric Power; Industrial and Cogeneation, 1997, Paper No. 97-GT-204, V003T09A038.

[4] Owen J.M., Roger R.H., Flow and heat transfer in rotating-disc systems: Flow & heat trans in rotat V1 CL (Mechanical engineering research studies: Engineering design series) (Volume 1). Wiley, 1989.

[5] Zimmermann H., Wolff K.H., Air system correlations: Part 1—Labyrinth seals. ASME 1998 International Gas Turbine and Aeroengine Congress and Exhibition. 1998, Paper No: 98-GT-206, V004T09A048.

[6] Da S.R., Facchini B., Innocenti L., Micio M., Analysis of gas turbine rotating cavities by a one-dimensional model: definition of new disk friction coefficient correlations set. Journal of Turbomachinery, 2011, 133(2): 021020.

[7] Coren D., Atkins N., Long C., Eastwood D., Childs P., Gujarro-Valencia A., Dixon J., The influence of turbine stator well coolant flow rate and passage configuration on cooling effectiveness. ASME 2011 Turbo Expo: Turbine Technical Conference and Exposition, 2011, Paper No. GT2011-46448, pp., 981–992.

[8] Simoni D., Zunino P., Lengani D., Guida R., Design and commissioning of a rotating turbine rig for cavity flows investigation. ISABE, 2017, Paper No. ISABE-2017 -21499.

[9] Kong X., Liu G., Liu Y., Feng Q., Investigation on the leakage flow, windage heating and swirl development of rotating labyrinth seal in a compressor stator well. ASME Turbo Expo 2016: Turbomachinery Technical Conference and Exposition, 2016, Paper No: GT2016-56740, V05AT15A014.

[10] Willenborg K., Kim S., Wittig S., Effects of Reynolds number and pressure ratio on leakage loss and heat transfer in a stepped labyrinth seal. Journal of Turbomachinery, 2001, 123(4): 815–822.

[11] Green B.R., Mathison R.M., Dunn M.G., Comparison of harmonic and time marching unsteady computational fluid dynamics solutions with measurements for a single-stage high-pressure turbine. Journal of Turbomachinery, 2013, 136(1): 011005.

[12] Hembera M., Loos A., Kührmann A., Danner F., Kau H., Johann E., Validation of the non-linear harmonic approach for quasi-unsteady simulations in turbomachinery. ASME Turbo Expo: Power for Land, Sea, and Air, 2009, Paper No. GT2009-59933, pp. 567–577.

[13] Schuler P., Kurz W., Dullenkopf K., Bauer H.-J., The influence of different rim seal geometries on hot-gas ingestion and total pressure loss in a low-pressure turbine. ASME Turbo Expo: Power for Land, Sea, and Air, 2010, Paper No. GT2010-22205, pp. 1123–1134.

[14] Andreini A., Da Soghe R., Facchini B., Zecchi S., Turbine stator well CFD studies: effects of cavity cooling air flow. ASME Turbo Expo: Power for Land, Sea, and Air, 2008, Paper No. GT2008-51067, pp. 2509–2521.

[15] Coren D.D., Atkins N.R., Long C.A., Eastwood D., Childs P.R.N., Guijarro-Valencia A., Dixon J.A., The influence of turbine stator well coolant flow rate and passage configuration on cooling effectiveness. ASME Turbo Expo: Power for Land, Sea, and Air, 2011, Paper No. GT2011-46448, pp. 981–992.

[16] Barakos G.N., Lawson S.J., Steijl R., Nayyar P., Numerical simulations of high-speed turbulent cavity flows. Flow, Turbulence and Combustion, 2009, 83(4): 569.

[17] Alexiou A., Long C.A., Turner A.B., Barnes C.J., Thermal Modelling of a rotating cavity rig to simulate the internal air system of a gas turbine HP compressor. 5th World Conference on Experimental Heat Transfer, Fluid Mechanics and Thermodynamics, ExHFT-5, 2001, 3: 2387–2392.

[18] Buron J.D., Houde S., Lestriez R., Deschênes C., Application of the non-linear harmonic method to study the rotor-stator interaction in Francis-99 test case. Journal of Physics: Conference Series, 2015, 579(1): 012013.

[19] Gao F., Poujol N., Chew J.W., Beard P.F., Advanced numerical simulation of turbine rim seal flows and consideration for RANS turbulence modeling. ASME Turbo Expo 2018: Turbomachinery Technical Conference and Exposition, 2018, Paper No. GT2018-75116, V05BT15A005.

[20] Guida R., Lengani D., Simoni D., Ubaldi M., Zunino P., New facility setup for the investigation of cooling flow, viscous and rotational effects on the interstage seal flow behavior of a gas turbine. ASME Turbo Expo 2018: Turbomachinery Technical Conference and Exposition, 2018, Paper No. GT2018-75630, V05BT15A017.

[21] NUMECA, User manuals. Academic R&D license, 2019.

[22] Menter F.R., Two-equation eddy-viscosity turbulence models for engineering applications. AIAA journal, 1994, 32(8): 1598–1605.

[23] Infantino D., Satta F., Simoni D., Ubaldi M., Zunino P., Bertini F., Analysis of a LPT rotor blade for a geared engine: Part II—Characterization of the time-varying flow field in a single stage research turbine. ASME Turbo Expo 2016: Turbomachinery Technical Conference and Exposition, 2016, Paper No. GT2016-57725, V02BT38A051.